Supplementary Information for

Facile fabrication of self-supporting porous nanosheets $CuMoO_4@Co_3O_4$ as bifunctional electrocatalyst for efficient overall water splitting

Fei Fei Dai [a], Yan Xue Xue [a], Ding Ling Gao [a], Yu Xiang Liu [a], Jian Hua Chen [a, b, *], Qiao Jing Lin [a], Wei Wei Lin [a], Qian Yang [a, b, *]

[a] College of Chemistry, Chemical Engineering and Environment, Minnan Normal University, Zhangzhou 363000, PR China.

[b]Fujian Province University Key Laboratory of Modern Analytical Science and Separation Technology, Minnan Normal University, Zhangzhou 363000, PR China.

[*]Corresponding author:

E-mail addresses and contact details: jhchen73@126.com (J.H.Chen); Tel: +86 0596 2591445; Fax: +86 0596 2520035(J.H. Chen); yangqian0417@163.com (Q.Yang).

1. Chemicals

The nickel foam was acquired from Longshengbao (Kunshan, China). Cobalt (II) nitrate hexahydrate [$Co(NO_3)_2 \cdot 6H_2O$], Pt-C (20 wt%) and cupric (II) nitrate hydrate [$Cu(NO_3)_2 \cdot 3H_2O$] were purchased from Mackun (Shanghai, China). Ammonium molybdate tetrahydrate [$(NH_4)_6Mo_7O_{24} \cdot 4H_2O$], N, N-Dimethylformamide [DMF, $(CH_3)_2NC(O)H$], potassium hydroxide (KOH), concentrated hydrochloric acid (HCl) and ethanol (C_2H_5OH) were purchased from Xilong Scientific. Iridium oxide powder (IrO_2, 99%) and Nafion were bought from Aladdin (Shanghai, China).

2. Materials characterization

The surface morphology, structure and chemical composition of the samples were determined by a scanning electron microscope (SEM, TESCAN MIRA-4) equipped with an energy-dispersive X-ray (EDX) spectroscopy. The nanostructure and crystallinity of the samples were characterized by transmission electron microscopy (TEM, FEI Tecnai G2 F20) and high-resolution transmission electron microscopy (HRTEM). The crystal phase and phase composition of samples were conducted by X-ray diffractometer (XRD, D8 Advance-X) with Cu Kα radiation and X-ray photoelectron spectroscopy (XPS, Thermo Scientific K-Alpha). The permeability between the electrode and electrolyte of the sample was characterized by a dynamic / static contact angle tester (SL200B). N_2 adsorption experiments were carried out on Mike ASAP2460 instrument. The metal concentration in the electrolyte after reaction was detected by inductively coupled plasma mass spectrometry (ICP-MS, Agilent 7500cx). Raman spectroscopy (Raman, LabRAM HR Evolution, France) was used to further investigate the molecular vibration.

3. Electrochemical tests

The electrochemical performance test was carried out on the CHI660E electrochemical workstation of Shanghai Chenhua Instrument Co., Ltd. Electrochemical measurements were carried out in a classic three-electrode setup with our self-made NF substrate electrode (1×1 cm^{-2}) as the working electrode, a graphite rod as the counter electrode, and a standard Hg/HgO (1 mol L^{-1} NaOH) electrode as the reference electrode. All measurements were performed in KOH (pH = 14) electrolyte with a concentration of 1 mol L^{-1}. In the test process of linear cyclic voltammetry (LSV), the polarization curves of OER and HER were obtained at the scanning rates of 2 mV s^{-1} and 5 mV s^{-1}, respectively. The potential obtained from the test needs to be converted to reversible hydrogen. Formula E *vs.* RHE = E *vs.* Hg / HgO + 0.098 + 0.059 pH is used to calibrate all potential as reversible hydrogen electrode (RHE). The relationship between overpotential (η) and current density logarithm ($\log j$) can be drawn by the test results of LSV curve with 100% IR compensation and the corresponding Tafel curve can be obtained. Electrochemical impedance spectroscopy (EIS) was measured in the frequency range of 10 kHz ~ 0.01 Hz and the amplitude of 5 mV. The stability of $CuMoO_4$@Co_3O_4/NF electrode was tested by cyclic voltammetry (CV) and chronopotentiometry (P-T), respectively and the scanning rate of cyclic voltammetry (CV) was 50 mV s^{-1}. ECSA of electrocatalysts were evaluated by measurement of cyclic voltammogram (CV) curves in the potential range of 0.924 V ~ 1.024 V (*vs* RHE) at different scan rates. According to the linear slope of sweep rate versus current density, their double-layer capacitance (C_{dl}) values were estimated. A two-electrode system was employed to assess the overall water electrolysis performance in 1 mol L^{-1} (M) KOH, and its stability was measured at a constant current density at 10 mA cm^{-2} for 120 h. In the presence of the heterogeneous catalyst, the turnover frequency (TOF) is calculated using (Eq.

(S1, S2)) [1]:

$$TOF\ (H_2,\ \text{for a heterogeneous catalyst}) = j / (2 \times F \times m) \quad (S1)$$

$$TOF\ (O_2,\ \text{for a heterogeneous catalyst}) = j / (4 \times F \times m) \quad (S2)$$

where j represents the current density at an overpotential, F represents the Faraday constant, m is the number of moles of metal on the electrode.

The Faradaic efficiency (FE) measured by drainage method at 100 mA cm^{-2} for 110 min and calculated by formula (Eq. (S3, S4)):

$$FE = V_{measured} / V_{calculated} \quad (S3)$$

$$V_{calculated} = (V_m \times Q) / (n \times F) \quad (S4)$$

where $V_{measured}$ represents the actual collected gas production, $V_{calculated}$ represents the theoretical gas production, V_m is the gas molar volume at room temperature and atmospheric pressure, Q is the total power consumption, n is the electron transfer number, and F is the Faraday constant.

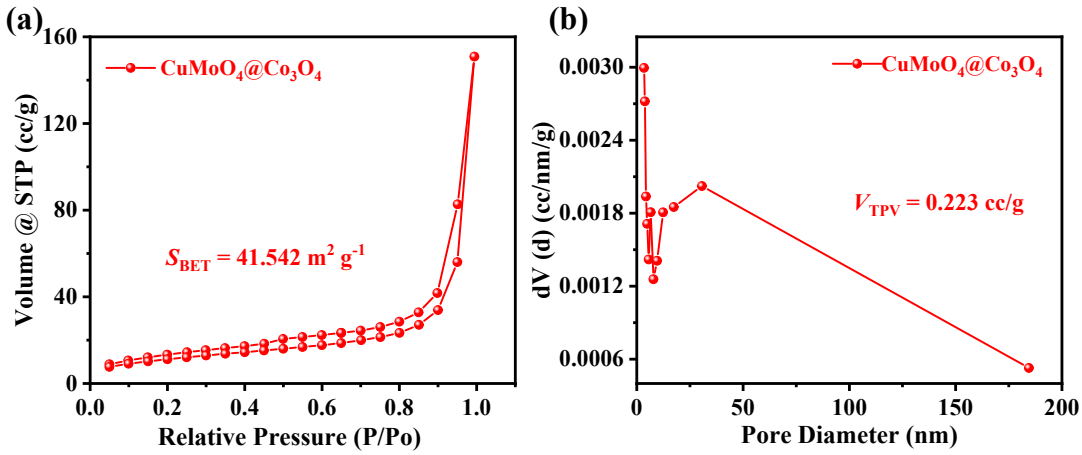

Fig. S1 (a) BET analysis and (b) Pore Distribution curve of $CuMoO_4@Co_3O_4$ catalyst.

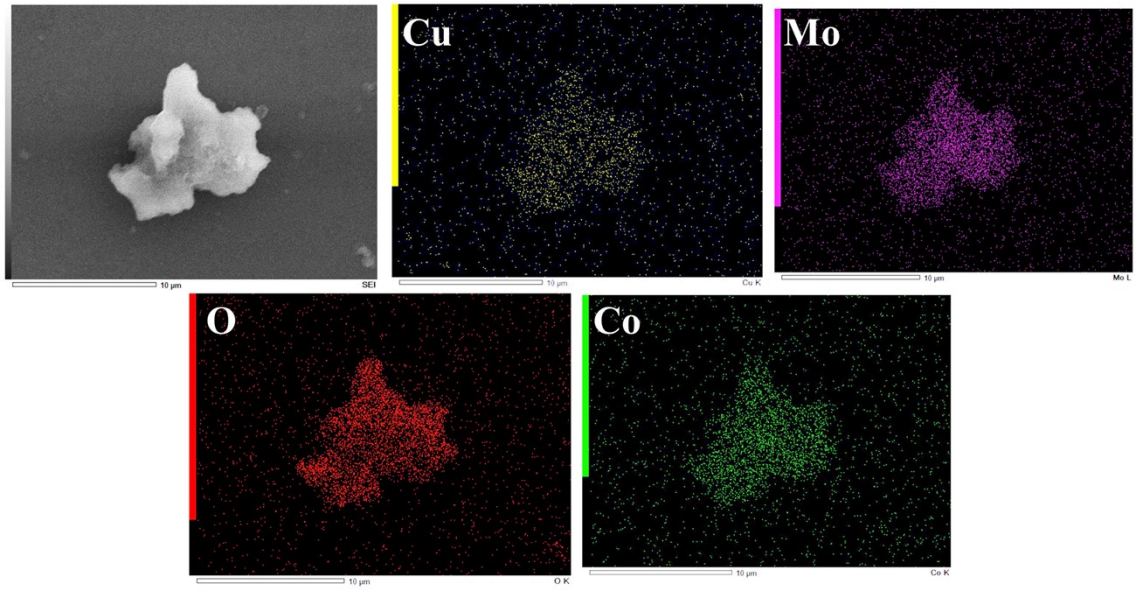

Fig. S2 Elemental mapping images of Cu, Mo, O, and Co of $CuMoO_4$@Co_3O_4 powders.

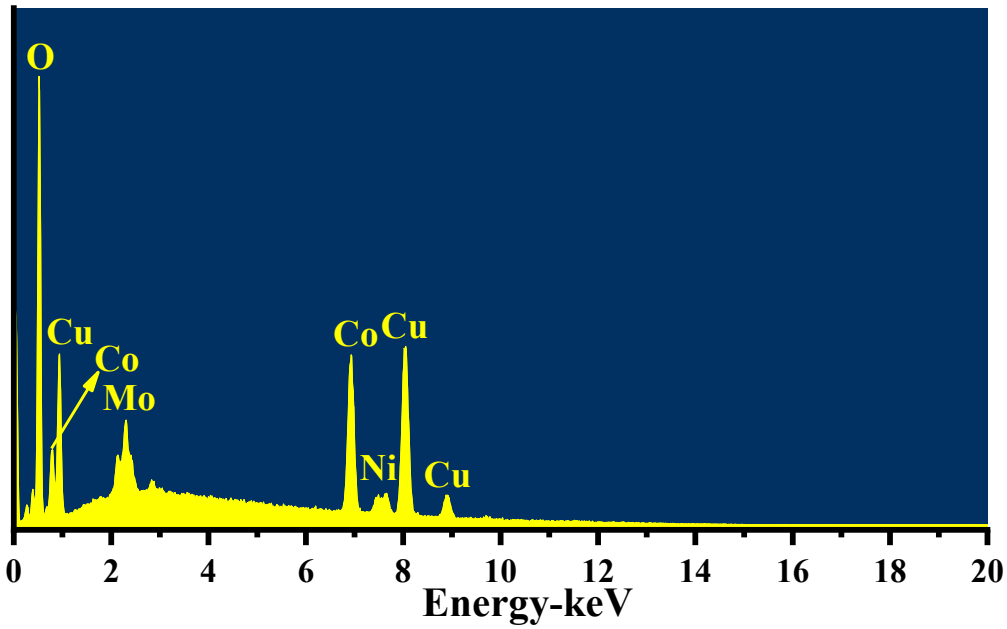

Fig. S3 EDS spectra of $CuMoO_4$@Co_3O_4/NF catalyst.

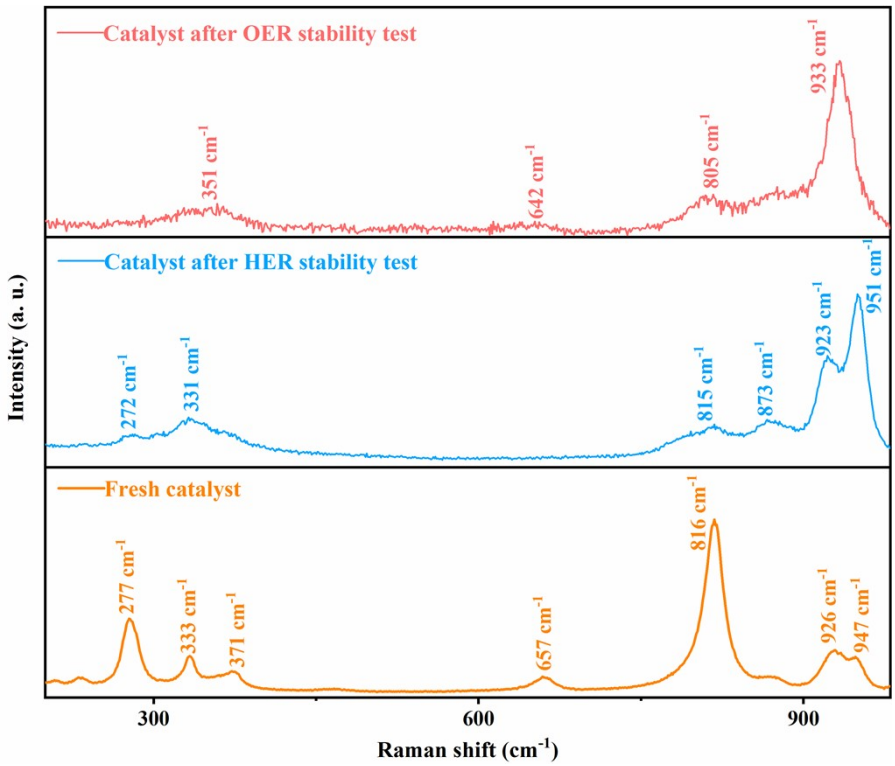

Fig. S4 The Raman spectrum of fresh catalyst, catalyst after HER stability test and catalyst after OER stability test.

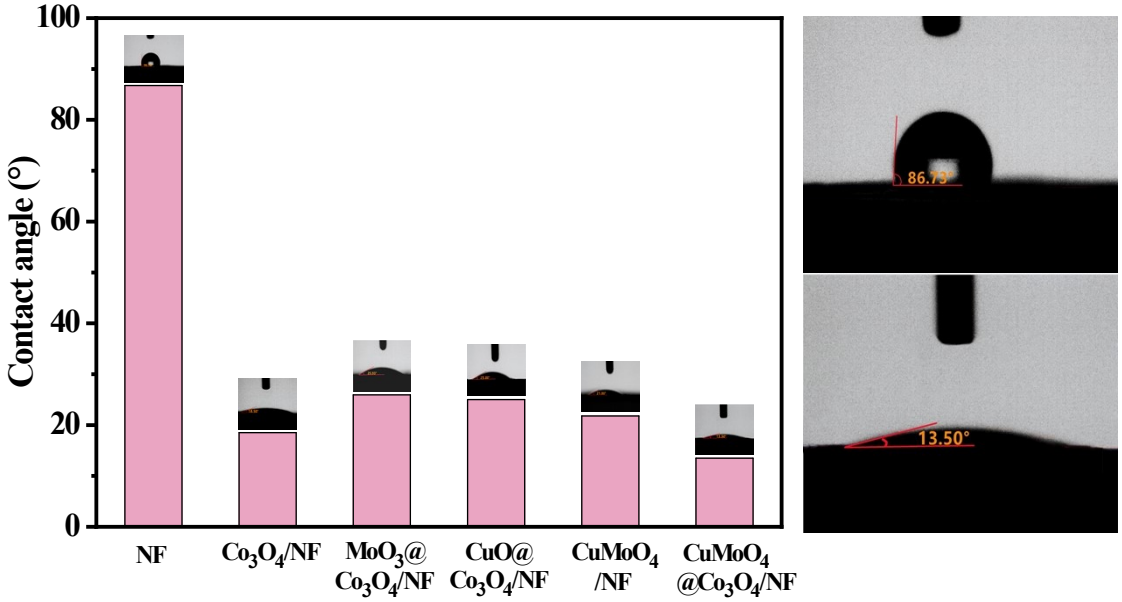

Fig. S5 Contact angle measurements of NF, Co_3O_4/NF, MoO_3@Co_3O_4/NF, CuO@Co_3O_4/NF, $CuMoO_4$/NF, $CuMoO_4$@Co_3O_4/NF.

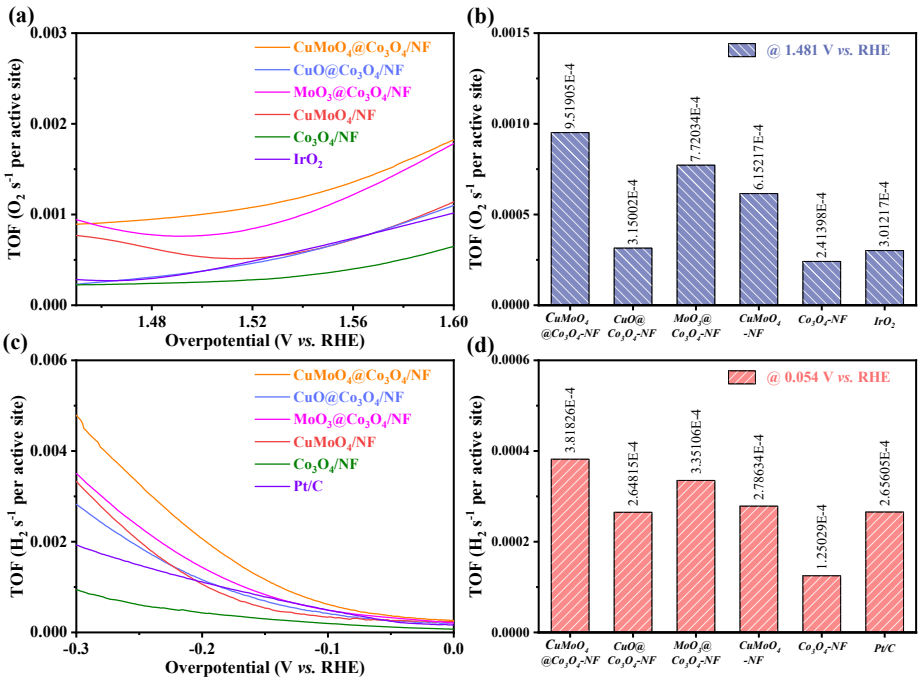

Fig. S6 （a, b）TOF diagrams of OER Overpotential on IrO_2, Co_3O_4/NF, MoO_3@Co_3O_4/NF, CuO@Co_3O_4/NF, $CuMoO_4$/NF and $CuMoO_4$@Co_3O_4/NF electrodes. (c, d) TOF diagrams of HER Overpotential on Pt/C, Co_3O_4/NF, MoO_3@Co_3O_4/NF, CuO@Co_3O_4/NF, $CuMoO_4$/NF and $CuMoO_4$@Co_3O_4/NF electrodes.

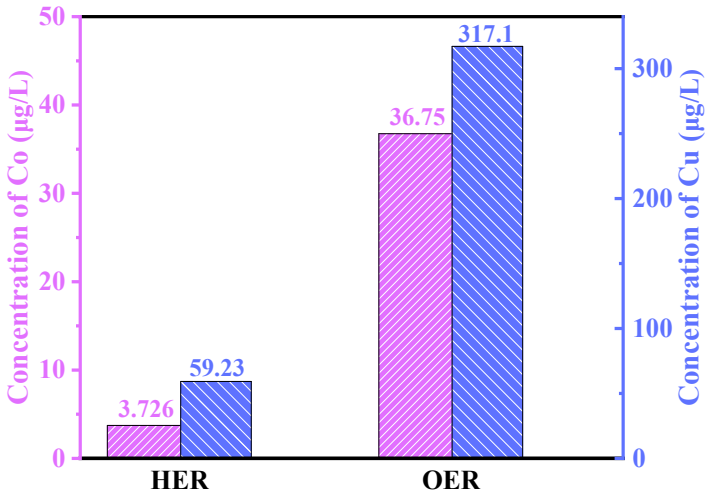

Fig. S7 The contents of Cu and Co released by HER and OER in the electrolyte after 2000 cycles of CV measured by ICP-MS.

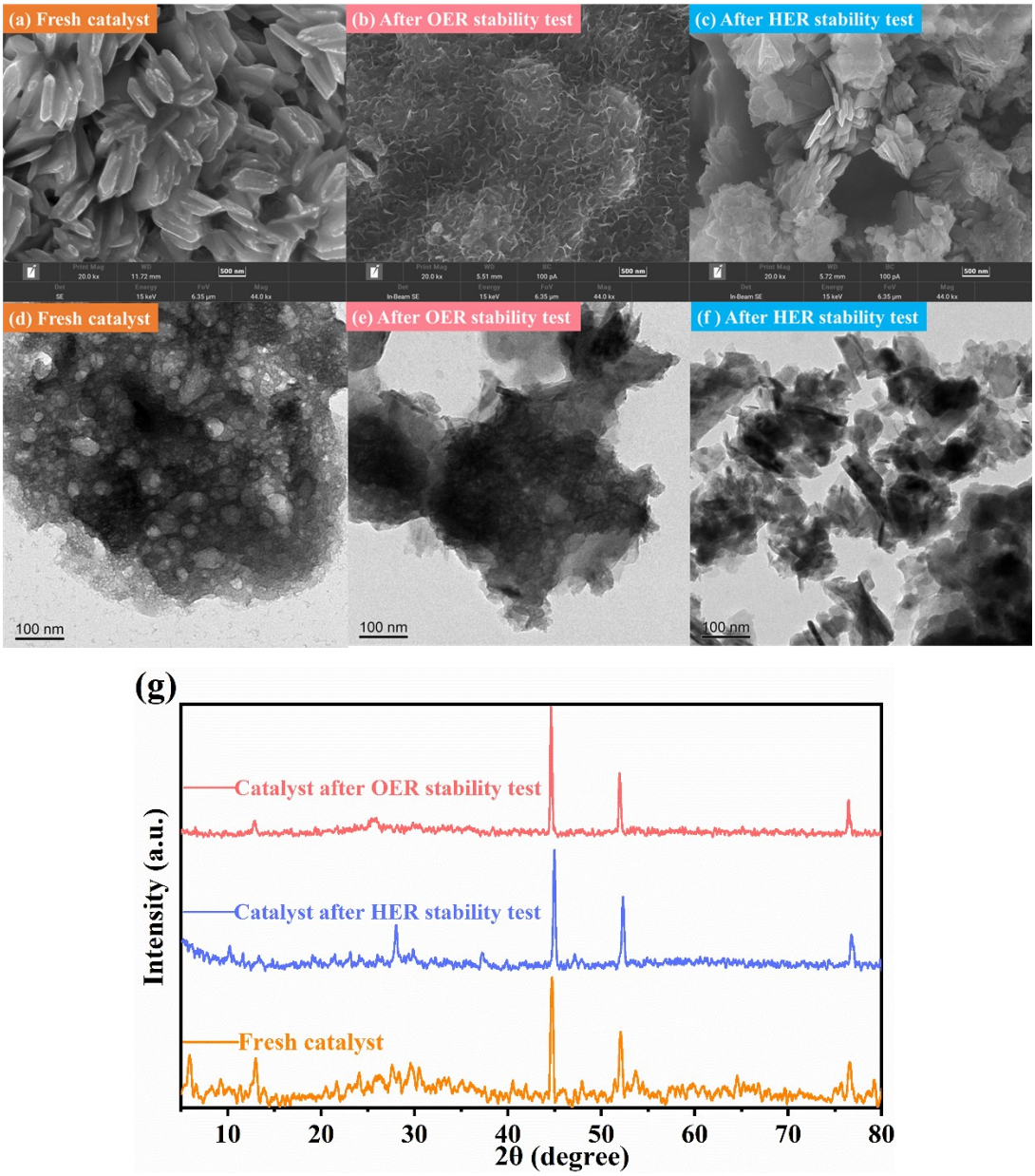

Fig. S8 (a-c) SEM pictures: (a)Fresh catalyst, (b) Catalyst after OER stability, (c) Catalyst after HER stability. (d-f) TEM pictures: (d)Fresh catalyst, (e) Catalyst after OER stability, (f) Catalyst after HER stability. (g)XRD patterns of fresh catalyst, catalyst after HER stability test and catalyst after OER stability test.

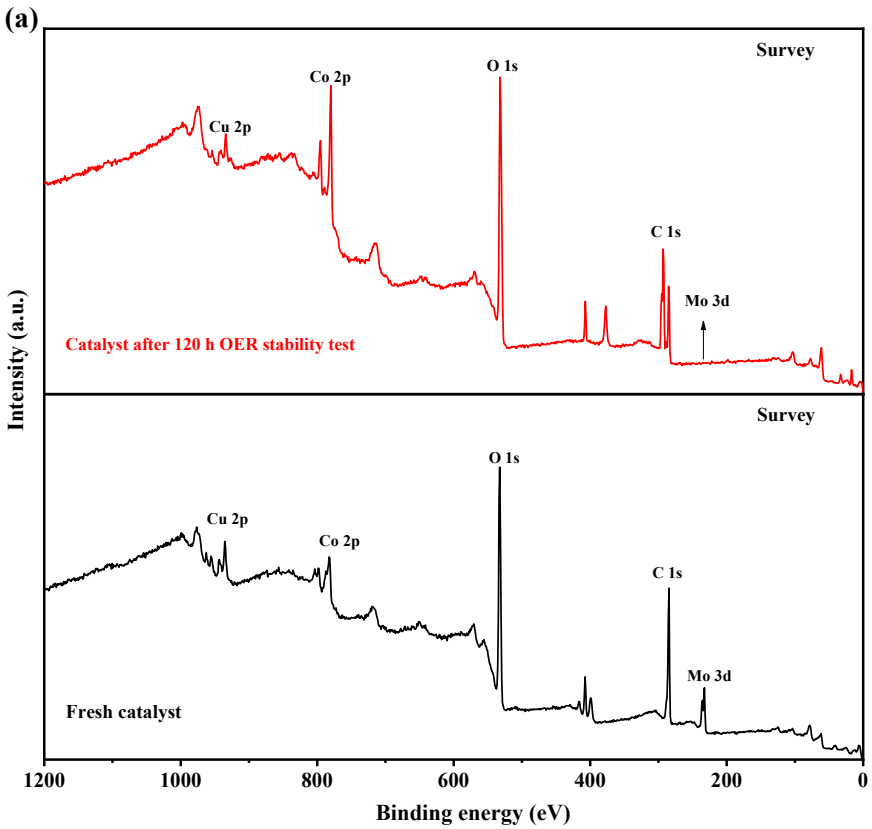
(a)
Survey
Co 2p
O 1s
Cu 2p
C 1s
Mo 3d
Catalyst after 120 h OER stability test
Survey
O 1s
Cu 2p
Co 2p
C 1s
Mo 3d
Fresh catalyst
Intensity (a.u.)
1200
1000
800
600
400
200
0
Binding energy (eV)

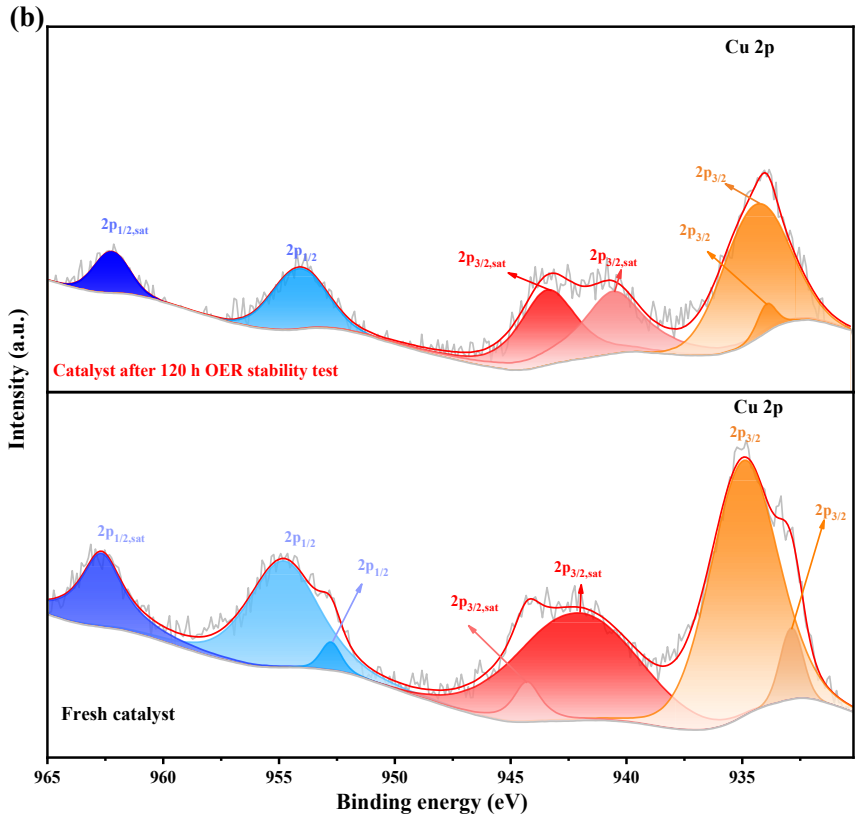
(b)
Cu 2p
2p1/2,sat
2p1/2
2p3/2,sat
2p3/2,sat
2p3/2
2p3/2
Catalyst after 120 h OER stability test
Cu 2p
2p3/2
2p1/2,sat
2p1/2
2p1/2
2p3/2,sat
2p3/2,sat
2p3/2
Fresh catalyst
Intensity (a.u.)
965
960
955
950
945
940
935
Binding energy (eV)

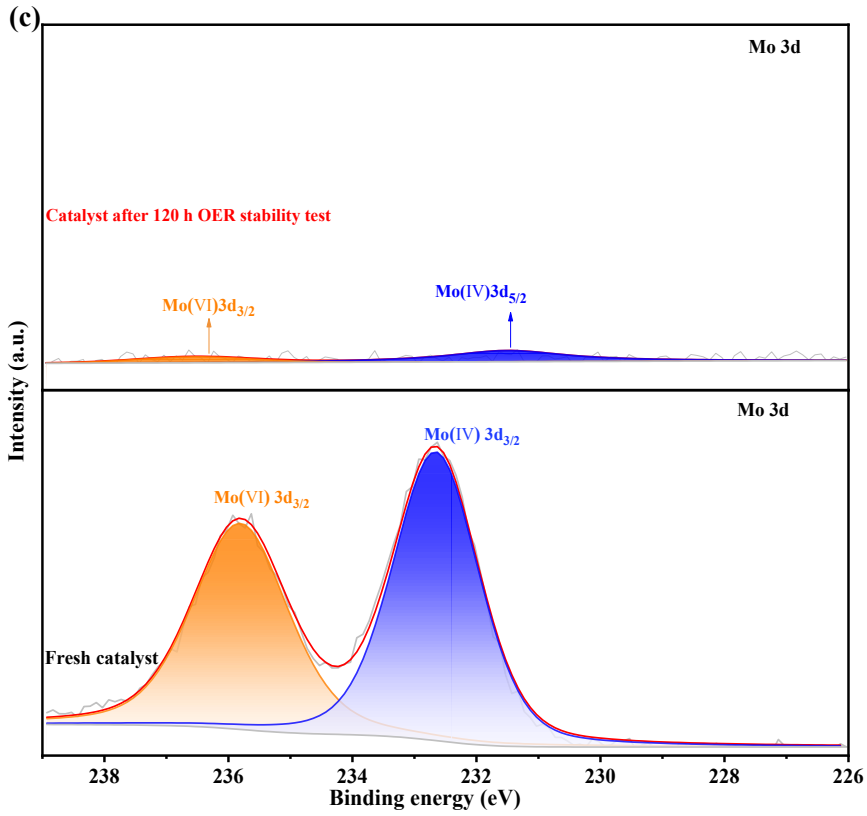
(c)
Mo 3d
Catalyst after 120 h OER stability test
Mo(VI)3d3/2
Mo(IV)3d5/2
Mo 3d
Mo(IV) 3d3/2
Mo(VI) 3d3/2
Fresh catalyst
Intensity (a.u.)
238
236
234
232
230
228
226
Binding energy (eV)

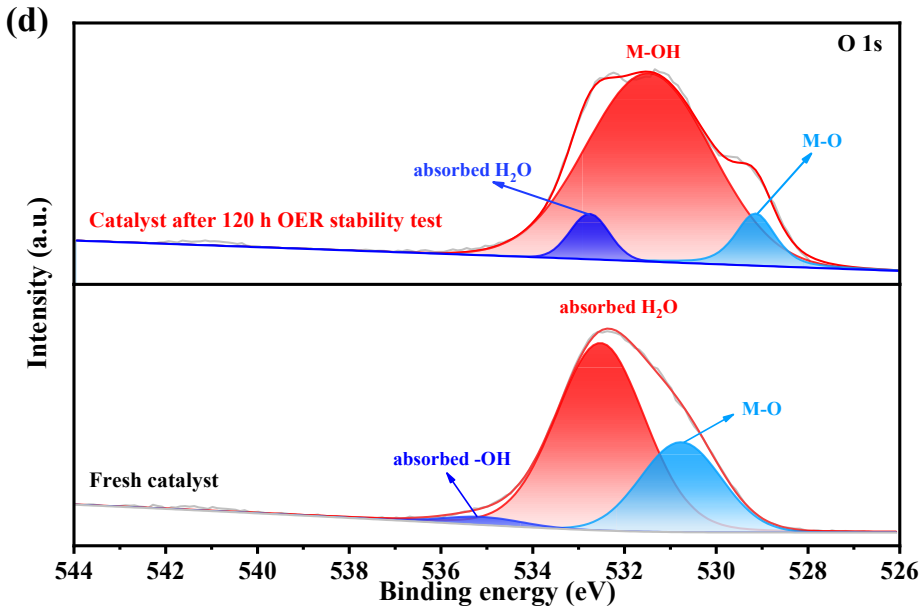
(d)
O 1s
M-OH
M-O
absorbed H2O
Catalyst after 120 h OER stability test
absorbed H2O
M-O
absorbed -OH
Fresh catalyst
Intensity (a.u.)
544
542
540
538
536
534
532
530
528
526
Binding energy (eV)

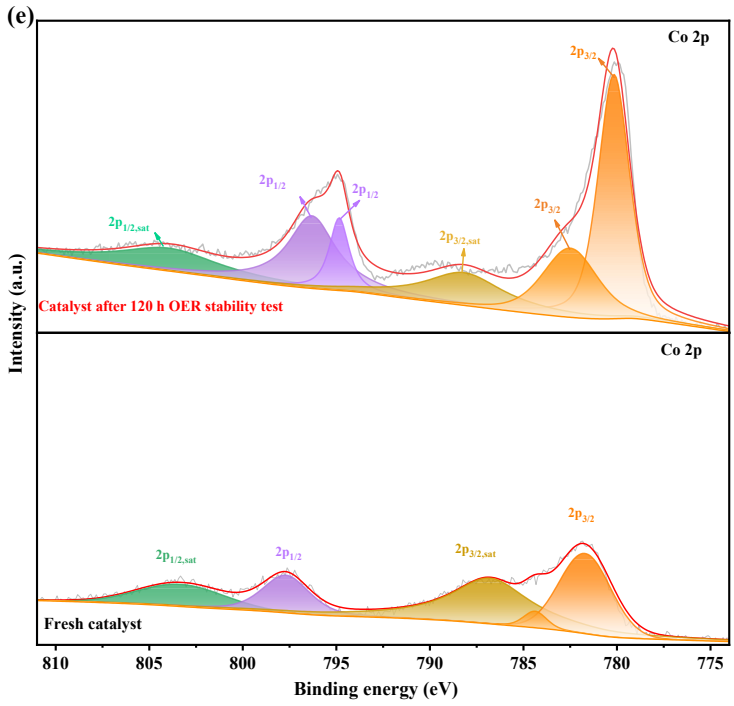

Fig. S9 XPS spectra. High-resolution XPS of (a) XPS survey, and b-e high-resolution XPS of (b) Cu 2p, (c) Mo 3d, (d) O 1s, and (e) Co 2p of the $CuMoO_4$@Co_3O_4/NF catalyst after 120 h OER stability tests.

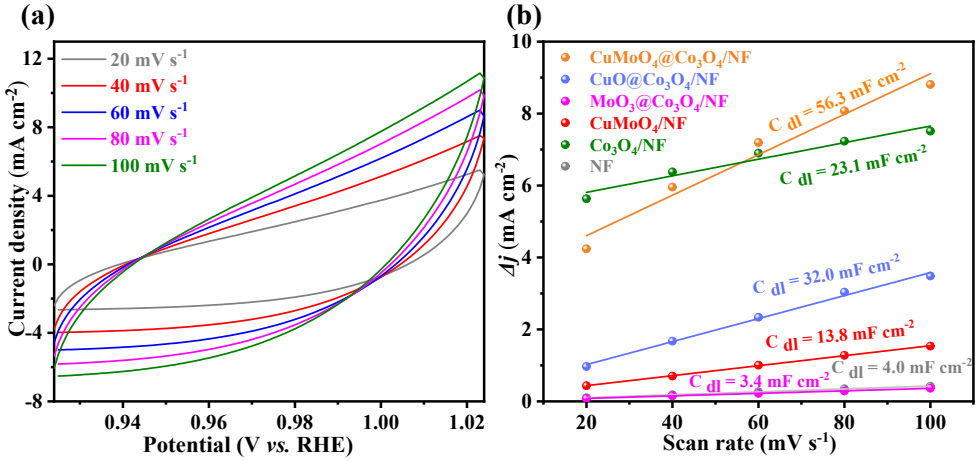

Fig. S10 (a) CV curves for calculation of double-layer capacitance. (b) Calculation of double-layer capacitance. CV curves of $CuMoO_4$@Co_3O_4/NF at scan rates ranging from 20 mV s^{-1} to 100 mV s^{-1} with an interval point of 20 mV s^{-1}. Linear fitting of the capacitive currents of the catalysts *vs.* the scan rates to calculate the double-layer capacitance (C_{dl}).

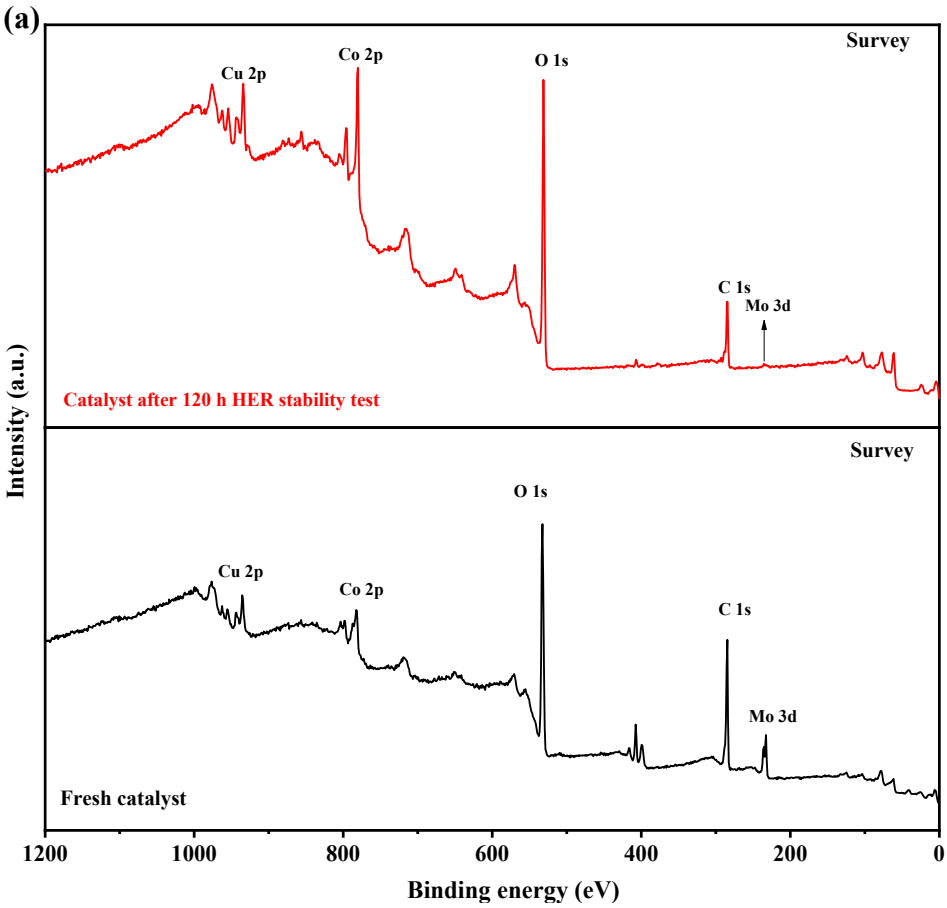
(a)
Survey
Cu 2p
Co 2p
O 1s
C 1s
Mo 3d
Catalyst after 120 h HER stability test
Survey
O 1s
Cu 2p
Co 2p
C 1s
Mo 3d
Fresh catalyst
Intensity (a.u.)
1200
1000
800
600
400
200
0
Binding energy (eV)

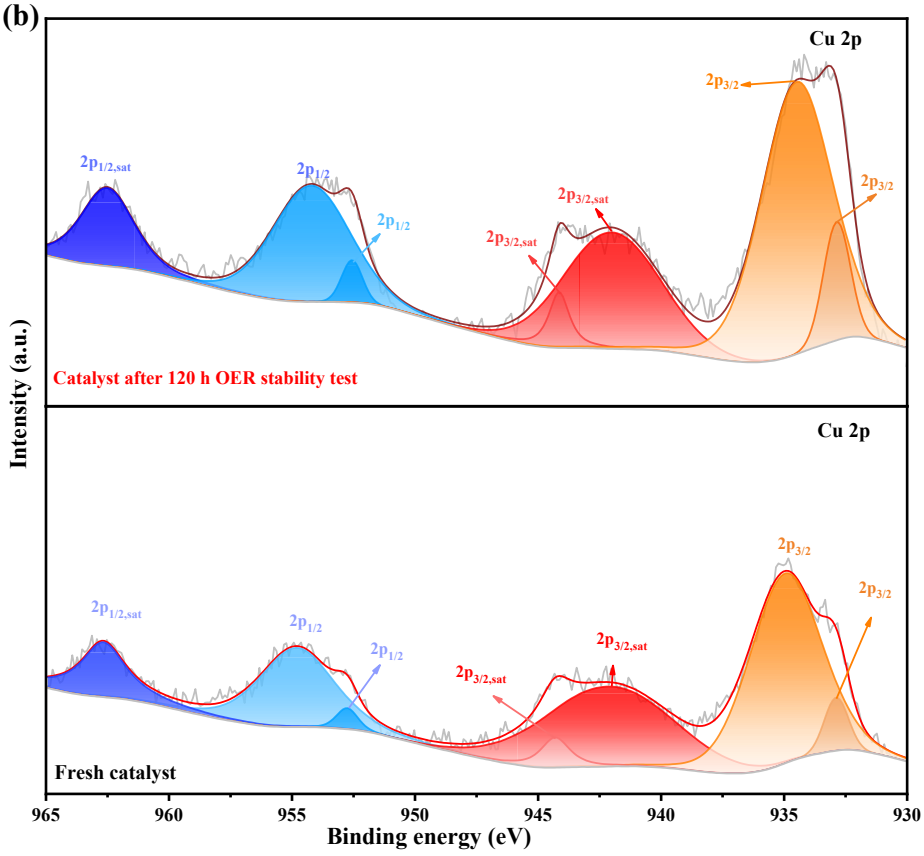
(b)
Cu 2p
2p3/2
2p1/2,sat
2p1/2
2p3/2,sat
2p3/2
2p1/2
2p3/2,sat
Catalyst after 120 h OER stability test
Cu 2p
2p3/2
2p1/2,sat
2p1/2
2p3/2,sat
2p3/2
2p1/2
2p3/2,sat
Fresh catalyst
Intensity (a.u.)
965
960
955
950
945
940
935
930
Binding energy (eV)

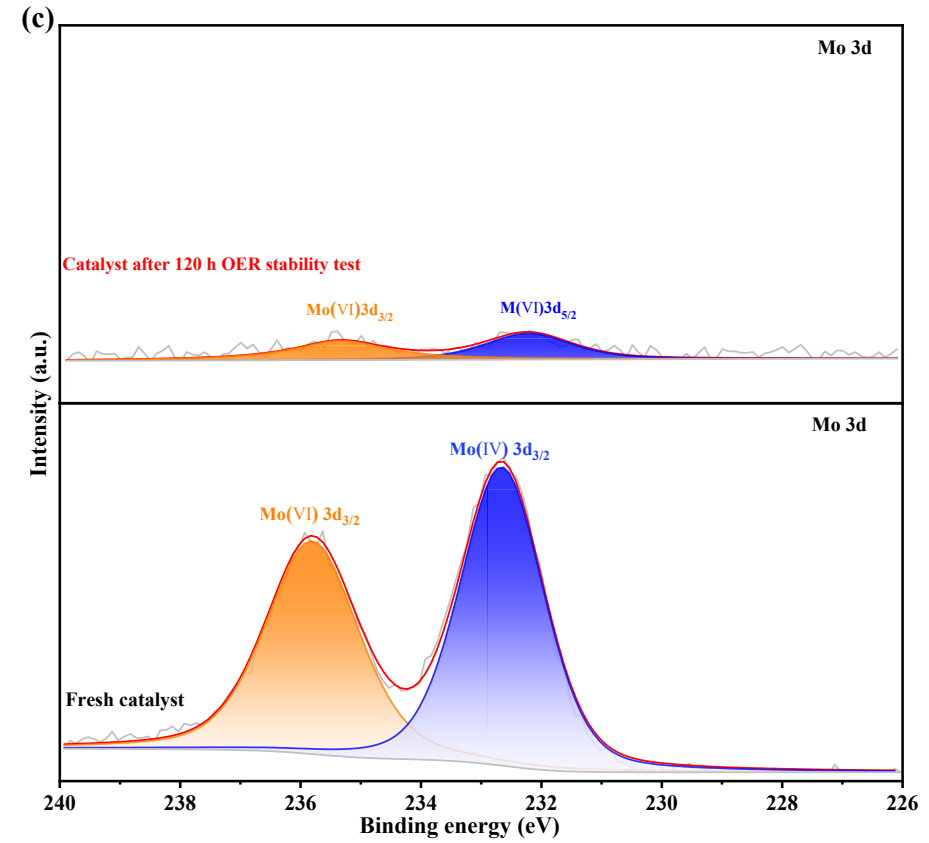
(c)
Mo 3d
Catalyst after 120 h OER stability test
Mo(VI)3d3/2
M(VI)3d5/2
Mo 3d
Mo(IV) 3d3/2
Mo(VI) 3d3/2
Fresh catalyst
Intensity (a.u.)
240
238
236
234
232
230
228
226
Binding energy (eV)

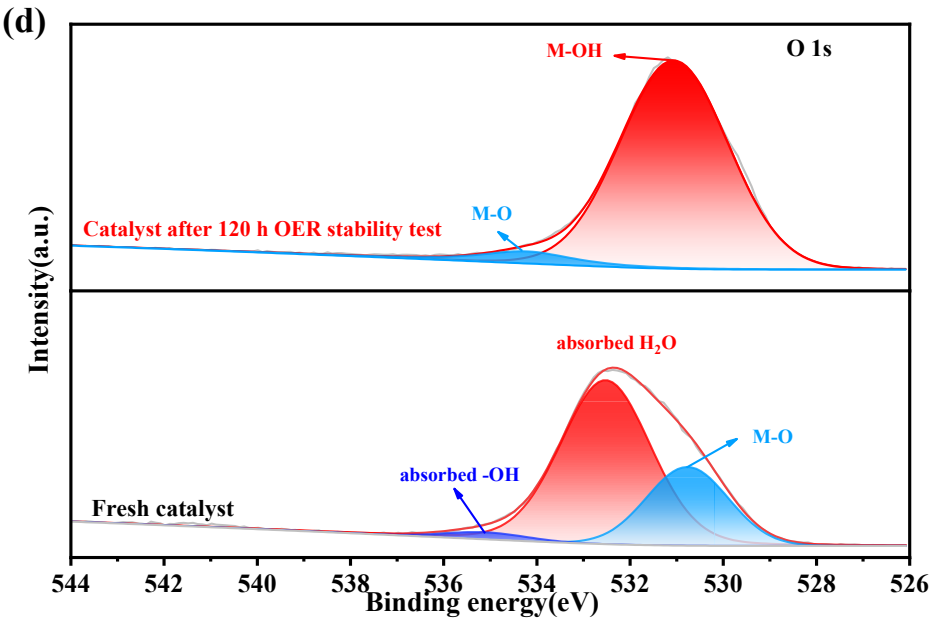
(d)
M-OH
O 1s
M-O
Catalyst after 120 h OER stability test
absorbed H2O
M-O
absorbed -OH
Fresh catalyst
Intensity(a.u.)
544
542
540
538
536
534
532
530
528
526
Binding energy(eV)

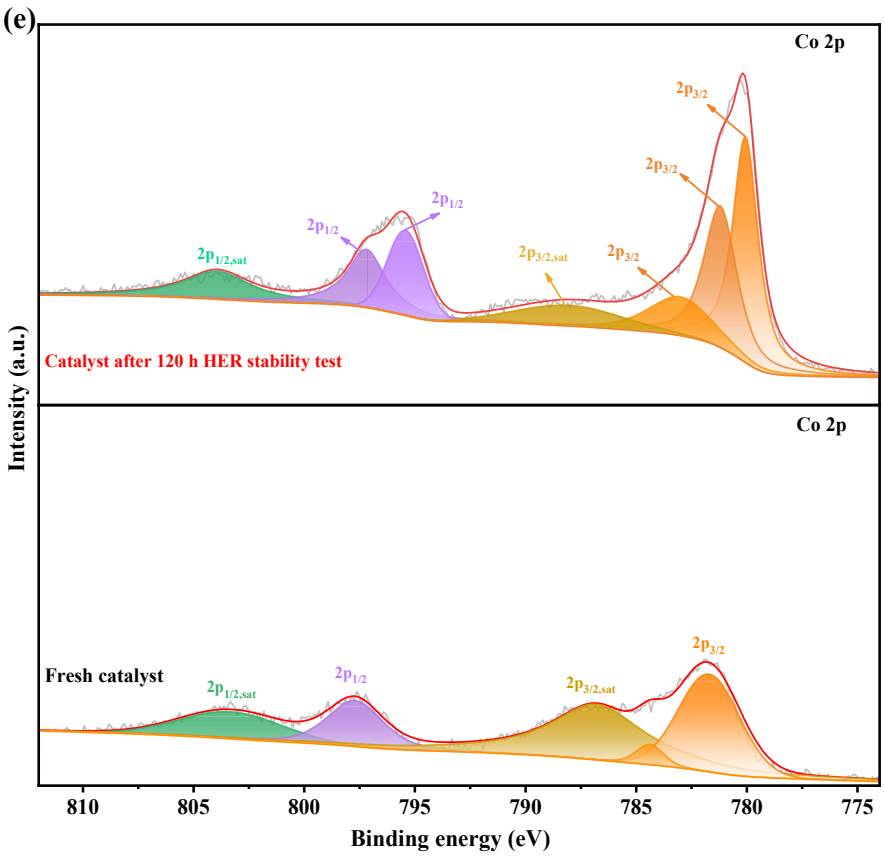

Fig. S11 XPS spectra. High-resolution XPS of (a) XPS survey, and b-e high-resolution XPS of (b) Cu 2p, (c) Mo 3d, (d) O 1s, and (e) Co 2p of the $CuMoO_4$@Co_3O_4/NF catalyst after 120 h HER stability tests.

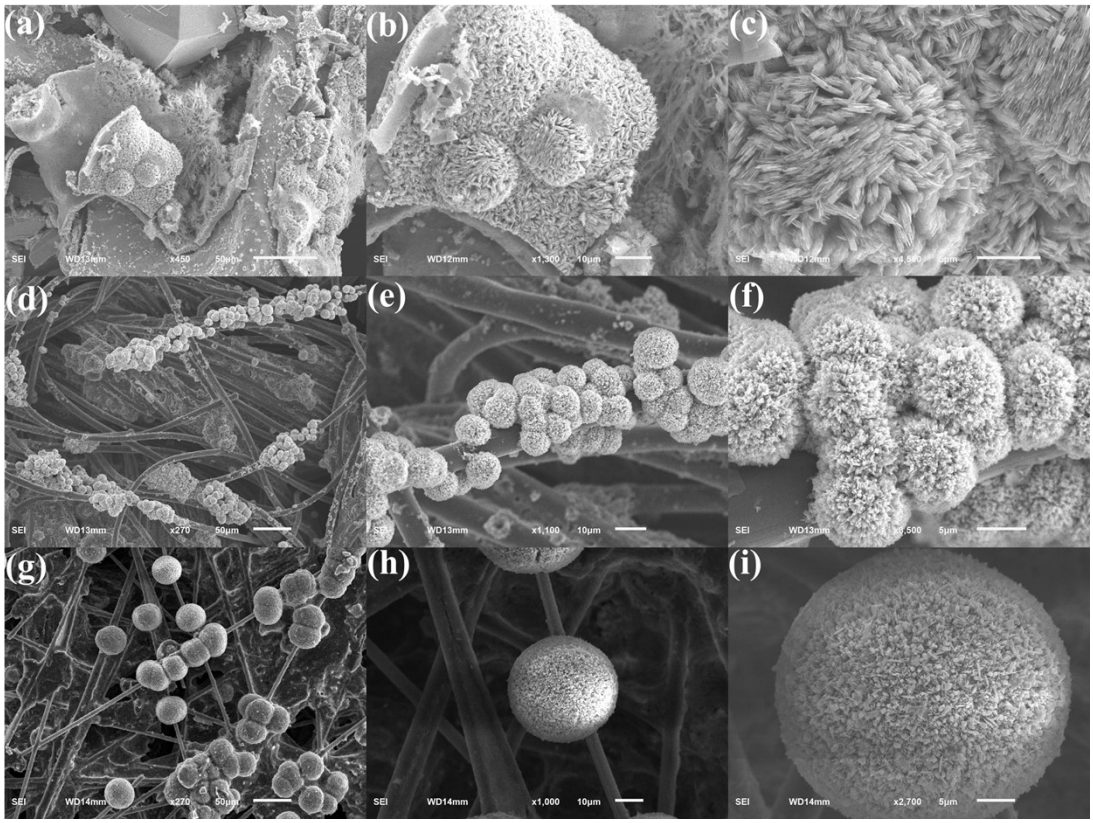

Fig. S12 SEM pictures: (a-c) $CuMoO_4@Co_3O_4$/CF, (d-f) $CuMoO_4@Co_3O_4$/CC and (g-i) $CuMoO_4@Co_3O_4$/CP.

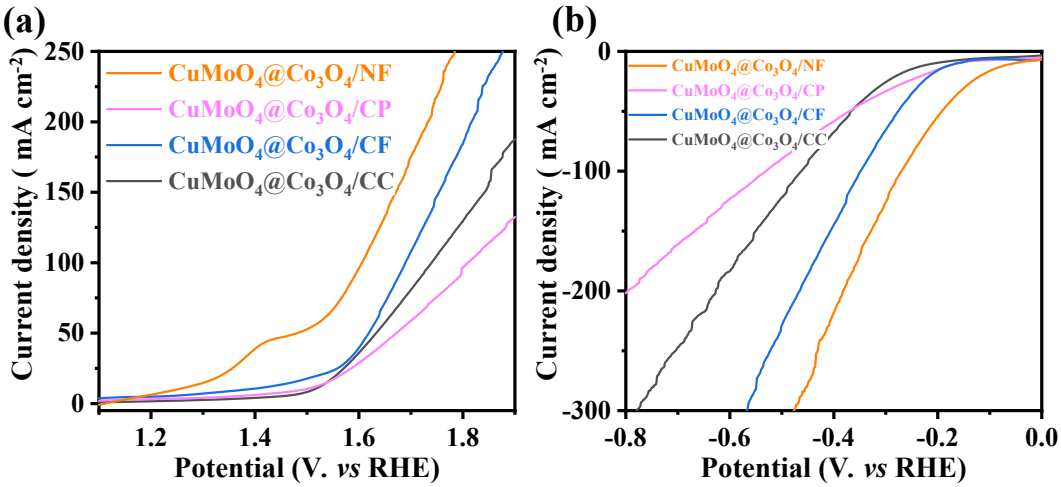

Fig. S13 OER and HER activities of $CuMoO_4@Co_3O_4$ catalysts prepared with different substrates in 1 mol L^{-1} KOH.

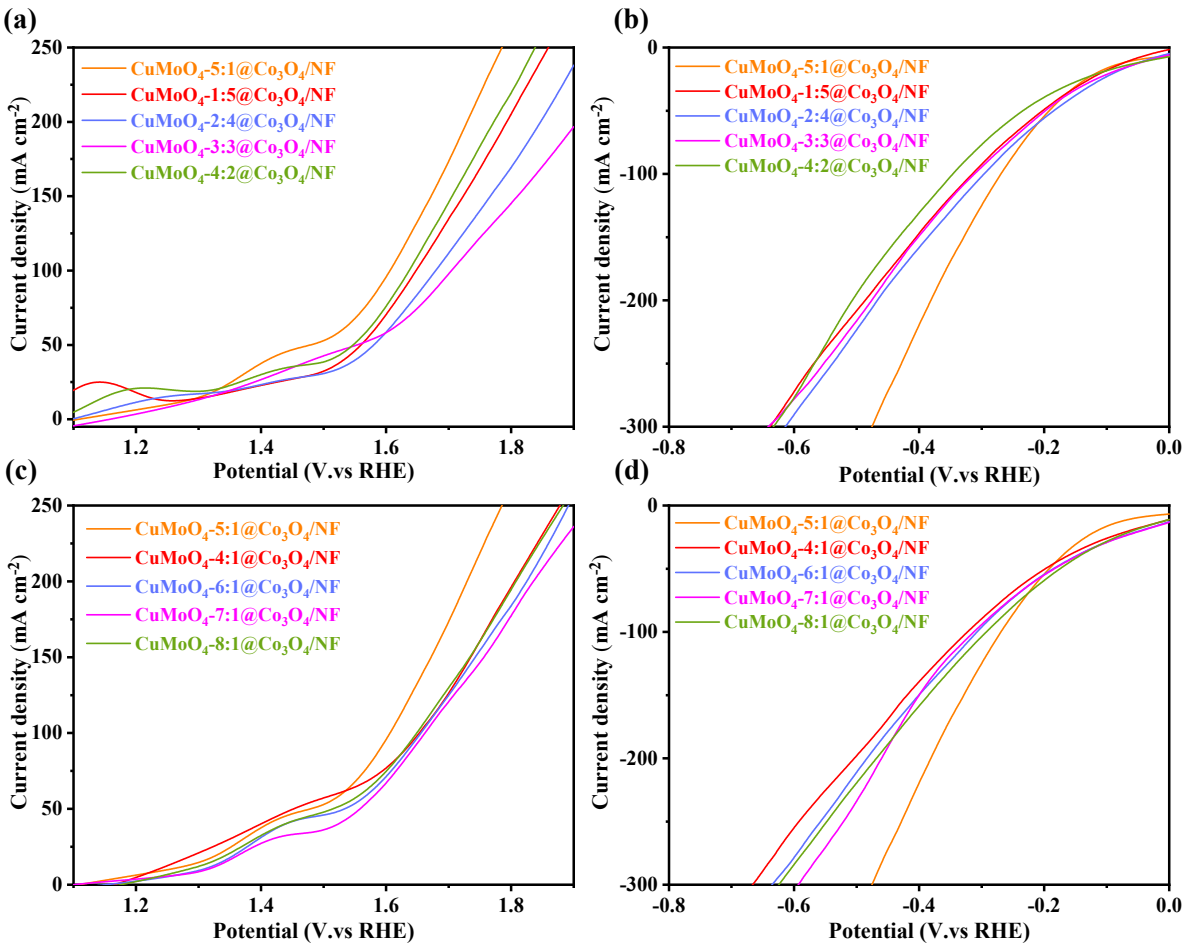

Fig. S14 OER and HER activities of $CuMoO_4@Co_3O_4$/NF catalysts prepared with different molar ratios of Cu and Mo in 1 mol L^{-1} KOH.

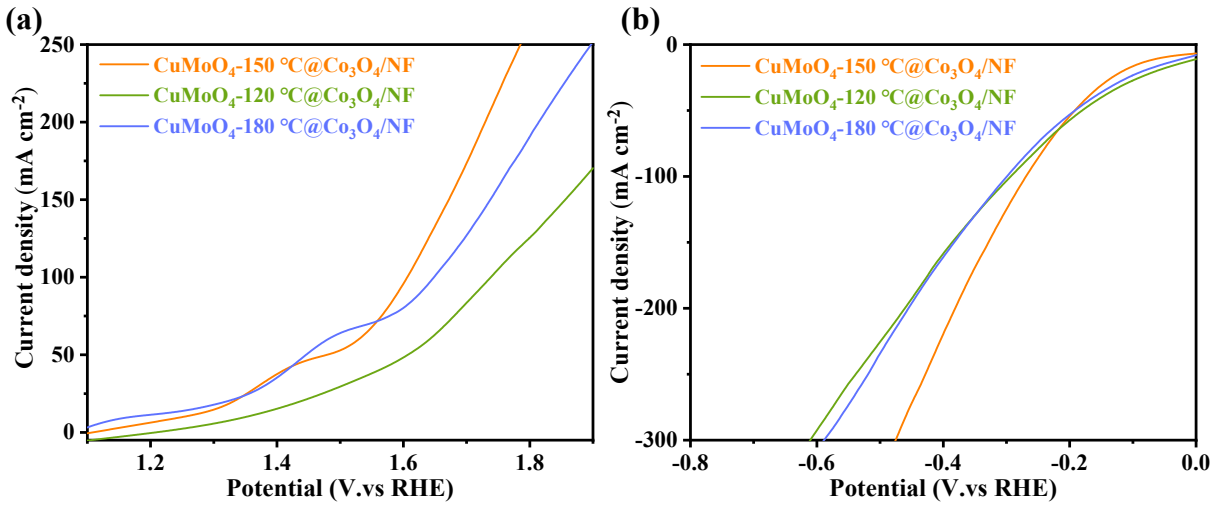

Fig. S15 OER and HER activities of $CuMoO_4@Co_3O_4$/NF catalysts prepared from $CuMoO_4$/NF precursors at different synthesis temperatures in 1 mol L^{-1} KOH.

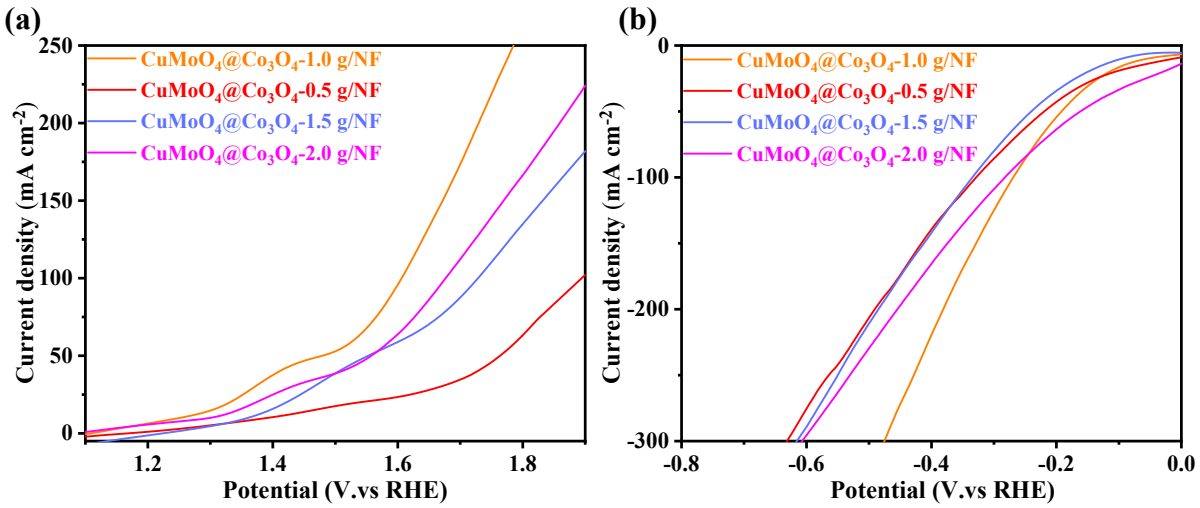

Fig. S16 OER and HER activities of $CuMoO_4@Co_3O_4$/NF catalysts prepared with different masses of cobalt nitrate hexahydrate in 1 mol L^{-1} KOH.

Table S1 The comparison of OER overpotentials of $CuMoO_4@Co_3O_4$/NF with other superior selected nonnoble catalysts.

Catalyst	Electrolyte	j (mA cm^{-2})	η (mV)	Reference
$CuMoO_4@Co_3O_4$/NF	1 mol L^{-1} KOH	50	251	This work
Cu-MoS_2-TS	0.5 mol L^{-1} H_2SO_4	50	273	2
NiCuP	1 mol L^{-1} KOH	50	300	3
Co-CuO	1 mol L^{-1} KOH	50	299	4
Cu_2S/C	1 mol L^{-1} KOH	10	410	5
Cu_3P/NF	1 mol L^{-1} KOH	10	290	6

Co-P/Cu	1 mol L^{-1} KOH	10	345	7
MoO_2/NF	1 mol L^{-1} KOH	10	250	8
MoNi	1 mol L^{-1} NaOH	10	290	9

Table S2 The comparison of HER overpotentials of $CuMoO_4$@Co_3O_4/NF with other superior selected nonnoble catalysts.

Catalyst	**Electrolyte**	***j*** **(mA** cm^{-2}**)**	***η*** **(mV)**	**Reference**
$CuMoO_4$@Co_3O_4/NF	1 mol L^{-1} KOH	-10	54	This work
$Mo_{0.25}Co_{0.75}P$	1 mol L^{-1} KOH	-10	59	10
Au/CoP@NC-3	1 mol L^{-1} KOH	-10	140.9	11
Cu/Mo_2C/Mo_2N	1 mol L^{-1} KOH	-10	82	12
Cu/Ni_3S_2	1 mol L^{-1} KOH	-10	128	13
Cu_3N	1 mol L^{-1} KOH	-10	118	14
Cu_3P@NF	1 mol L^{-1} KOH	-10	105	15
Mo_2C	1 mol L^{-1} KOH	-10	130	16
Cu_2Se@NiFe-LDHNS	1 mol L^{-1} KOH	-10	195	17
RhCu	1 mol L^{-1} KOH	-10	78	18
Cu_1Ni_2-N	1 mol L^{-1} KOH	-10	71	19
Pt/CoSe	1 mol L^{-1} KOH	-10	58	20
Co_3Mo/MoO_x/Ni	1 mol L^{-1} KOH	-10	68	21

Table S3 Comparisons of overall water-splitting performance of $CuMoO_4@Co_3O_4$/NF with some recently reported catalysts in 1.0 mol L^{-1} KOH.

Catalyst	Support	*j* (mA cm^{-2})	Voltage (V)	Reference
$CuMoO_4@Co_3O_4$/NF // $CuMoO_4@Co_3O_4$/NF	Ni Foam	10	1.51	This work
Cu_2Se@NiFe-LDHNS/CF // Cu_2Se@NiFe-LDHNS/CF	Cu Foam	10	1.667	17
CuO_x NWs@$NiMnO_x$ NSs/CF // CuO_x NWs@$NiMnO_x$ NSs/CF	Cu Foam	10	1.62	22
Cu_2S@Cu // Cu_2S@Cu	Cu Foam	10	1.84	23
Cu_3P/NF // Cu_3P/NF	Ni Foam	10	1.67	15
NiFe LDH@NiCoP/NF // NiFe LDH@NiCoP/NF	Ni Foam	10	1.57	24
Cu_3N // Cu_3N	Ni Foam	10	1.60	14
Co_3S_4/MOF // Co_3S_4/MOF	Conductive carbon cloth	10	1.55	25
CoFeZr oxides // CoFeZr oxides	Ni Foam	10	1.63	26
$NiCo_2S_4$ // $NiCo_2S_4$	Ni Foam	10	1.58	27

Table S4 The actual volume of H_2 collected by the drainage method and its associated Faradaic efficiency.

Time (s)	$V_{measured}$ (L)	$V_{calculated}$ (L)	FE (%)
600	0.0075	0.0076	98.5
1200	0.015	0.0152	98.5
1800	0.022	0.0229	96.3
2400	0.0295	0.0305	96.8
3000	0.0371	0.0381	97.4
3600	0.0447	0.0457	97.8
4200	0.0522	0.0533	97.9
4800	0.06	0.0609	98.5
5400	0.0675	0.0686	98.5
6000	0.075	0.0762	98.5
6600	0.0832	0.0838	99.3

Table S5 The actual volume of O_2 collected by the drainage method and its associated Faradaic efficiency.

Time (s)	$V_{measured}$ (L)	$V_{calculated}$ (L)	FE (%)
600	0.0036	0.0038	94.5
1200	0.007	0.0076	91.9
1800	0.0105	0.0114	91.9
2400	0.0143	0.0152	93.9
3000	0.0183	0.0190	96.1
3600	0.0223	0.0229	97.6
4200	0.0262	0.0267	98.3
4800	0.0302	0.0305	99.1
5400	0.0341	0.0343	99.5
6000	0.038	0.0381	99.8
6600	0.0415	0.0419	99.1

Notes and references

1 Z. Abdi, M. Vandichel, A. S. Sologubenko, M.-G. Willinger, J.-R. Shen, S. I. Allakhverdiev and M. M. Najafpour, *Int. J. Hydrogen Energy*, 2021, **46**, 37774-37781.

2 M. D. Sharma, C. Mahala, B. Modak, S. Pande and M. Basu, *Langmuir*, 2021, **37**, 4847-4858.

3 L. Wei, K. Goh, O. Birer, H. E. Karahan, J. Chang, S. Zhai, X. Chen and Y. Chen, *Nanoscale*, 2017, **9**, 4401-4408.

4 X. Xiong, C. You, Z. Liu, A. M. Asiri and X. Sun, *ACS Sustainable Chem. Eng.*, 2018, **6**, 2883-2887.

5 X. Zhao, L. Liu, Y. Zhang, H. Zhang and Y. Wang, *Nanotechnol.*, 2017, **28**, 345402.

6 J. Hao, W. Yang, Z. Huang and C. Zhang, *Adv. Mater. Interfaces*, 2016, **3**, 1600236.

7 N. Jiang, B. You, M. Sheng and Y. Sun, *Angew. Chem. Int. Ed. Engl.*, 2015, **54**, 6251-6254.

8 Y. Jin, H. Wang, J. Li, X. Yue, Y. Han, P. K. Shen and Y. Cui, *Adv. Mater.*, 2016, **28**, 3785-3790.

9 J.M. Jaksˇic´ a, M.V. Vojnovic´ b , N.V. Krstajic´ b, *Electrochim. Acta.*, 2000, **45**, 4151-4158.

10 Y. Zhang, Z. Wang, F. Du, H. He, A. Alsaedi, T. Hayat, T. Li, G.-L. Li, Y. Zhou and Z. Zou, *J. Mater. Chem. A*, 2019, **7**, 14842-14848.

11 X. Wang, Y. Fei, W. Li, L. Yi, B. Feng, Y. Pan, W. Hu and C. M. Li, *ACS Appl. Mater. Interfaces*, 2020, **12**, 16548-16556.

12 R. Kumar, Z. Ahmed, H. Kaur, C. Bera and V. Bagchi, *Catal. Sci. Technol.*, 2020, **10**, 2213-2220.

13 J. X. Feng, J. Q. Wu, Y. X. Tong and G. R. Li, *J Am. Chem. Soc.*, 2018, **140**, 610-617.

14 C. Panda, P. W. Menezes, M. Zheng, S. Orthmann and M. Driess, *ACS Energy Lett.*, 2019, **4**, 747-754.

15 A. Han, H. Zhang, R. Yuan, H. Ji and P. Du, *ACS Appl. Mater. Interfaces*, 2017, **9**, 2240-2248.

16 L. Liao, S. Wang, J. Xiao, X. Bian, Y. Zhang, M. D. Scanlon, X. Hu, Y. Tang, B. Liu and H. H. Girault, *Energy Environ. Sci.*, 2014, **7**, 387-392.

17 H. Qi, P. Zhang, H. Wang, Y. Cui, X. Liu, X. She, Y. Wen and T. Zhan, *J. Colloid Interface Sci.*, 2021, **599**, 370-380.

18 D. Cao, H. Xu and D. Cheng, *Adv. Energy Mater.*, 2020, **10**, 1903038.

19 Z. Wang, L. Xu, F. Huang, L. Qu, J. Li, K. A. Owusu, Z. Liu, Z. Lin, B. Xiang, X. Liu, K. Zhao, X. Liao, W. Yang, Y. B. Cheng and L. Mai, *Adv. Energy Mater.*, 2019, **9**, 1900390.

20 K. Jiang, B. Liu, M. Luo, S. Ning, M. Peng, Y. Zhao, Y. R. Lu, T. S. Chan, F. M. F. de Groot and Y. Tan, *Nat. Commun.*, 2019, **10**, 1743-1752.

21 J. Chen, Y. Ge, Q. Feng, P. Zhuang, H. Chu, Y. Cao, W. R. Smith, P. Dong, M. Ye and J. Shen, *ACS Appl. Mater. Interfaces*, 2019, **11**, 9002-9010.

22 S. Sirisomboonchai, X. Li, N. Kitiphatpiboon, R. Channoo, S. Li, Y. Ma, S. Kongparakul, C. Samart, A. Abudula and G. Guan, *J. Mater. Chem. A*, 2020, **8**, 16463-16476.

23 B. Ma, Z. Yang, Z. Yuan and Y. Chen, *Int. J. Hydrogen Energy*, 2019, **44**, 1620-1626.

24 Y. Li, Y. Sun, Y. Qin, W. Zhang, L. Wang, M. Luo, H. Yang and S. Guo, *Adv. Energy Mater.*, 2020, **10**, 1903120.

25 T. Liu, P. Li, N. Yao, T. Kong, G. Cheng, S. Chen and W. Luo, *Adv. Mater.*, 2019, **31**, e1806672.

26 L. Huang, D. Chen, G. Luo, Y. R. Lu, C. Chen, Y. Zou, C. L. Dong, Y. Li and S. Wang, *Adv. Mater.*, 2019, **31**, e1901439.

27 Z. Kang, H. Guo, J. Wu, X. Sun, Z. Zhang, Q. Liao, S. Zhang, H. Si, P. Wu, L. Wang and Y. Zhang, *Adv. Funct. Mater.*, 2019, **29**, 1807031.